Annals of Glaciology

Article

Cite this article: Zhang Q, Li F, Lei J, Zhang S, Ding Z, Chen W, Li W (2020). Freeboard height and snow depth observed by floating GPS on land-fast sea ice in Nella Fjord, Antarctica. *Annals of Glaciology* **61**(82), 227–239. https://doi.org/10.1017/aog.2020.41

Received: 29 September 2019
Revised: 13 May 2020
Accepted: 14 May 2020
First published online: 16 June 2020

Key words:
GPS; sea-ice freeboard; sea-ice thickness; snow depth

Author for correspondence:
Jintao Lei, E-mail: jintao.lei@whu.edu.cn

cambridge.org/aog

Freeboard height and snow depth observed by floating GPS on land-fast sea ice in Nella Fjord, Antarctica

Qingchuan Zhang[1], Fei Li[1], Jintao Lei[1,2], Shengkai Zhang[1], Zhuoming Ding[3], Wu Chen[2] and Wenhao Li[1]

[1]Chinese Antarctic Centre of Surveying and Mapping, Wuhan University, Wuhan, China; [2]Department of Land Surveying and Geo-informatics, The Hong Kong Polytechnic University, Hong Kong, China and [3]National Marine Environmental Forecasting Center (NMEFC), Beijing, China

Abstract

Although altimeters have been widely used to monitor the spatiotemporal variation of sea-ice thickness, they are unable to separate sea-ice freeboard from snow depth. We use a floating GPS deployed on sea ice to derive the freeboard and snow depth near China's Zhongshan Station. Our results show that the standalone floating GPS can monitor freeboard with a precision of 4.2 cm. If time-varying dynamic ocean topography provided by, for example, a bottom pressure gauge is available, then the precision of GPS-derived freeboard can improve to 1.3 cm. The daily snow depth inverted by GPS interferometric reflectometry captures three precipitation events during our experiment, showing that the floating GPS can monitor the variation in snow depth and observe the freeboard variation at the same time. By studying the relationship between freeboard, snow depth and sea-ice thickness, we find that sea-ice thickness will be greatly underestimated by the negative single-point freeboard under the assumption of hydrostatic equilibrium. As a supplement to existing technologies, the GPS-derived freeboard and snow depth can be used both to evaluate the altimeter observations directly and to improve our understanding of the real-time variation of freeboard and snow depth in the experimental area.

1. Introduction

Permanent and seasonal sea ice covers ~7% of the entire Earth's surface (Wadhams, 2014). Sea ice stores and releases heat and fresh water as it grows and shrinks, affecting energy and salt budgets, sea-water composition, and ocean currents at high latitudes (Armitage and Ridout, 2015). Changes in sea-ice extent and thickness are important components of climate change (Screen and Simmonds, 2010). Arctic sea ice has declined in both extent and thickness over the past four decades, while for Antarctic sea ice, a dramatic decrease of extent began in late 2015 after nearly three decades of observed increasing trends (Cavalieri and Parkinson, 2008; Parkinson and DiGirolamo, 2016; Meehl and others, 2019). There are many potential reasons for the contrasts between changes in Arctic and Antarctic sea ice (Comiso and Nishio, 2008; Maksym, 2019). First, in contrast to the land-constrained Arctic sea ice, Antarctic sea ice grows unbounded at its northern edge and is mainly composed of seasonal sea ice (Antarctic sea-ice extent in summer is ~15% of that in winter). Antarctic sea ice is thin and more sensitive and vulnerable to thermodynamic forcing (such as regional warming, atmospheric/oceanic heat exchange and ice-albedo feedback) and dynamic forcing (such as wind and oceanic currents) (Zhang and others, 2012). Second, simulations indicate that global warming may lead to increased precipitation over the Southern Ocean, reducing the oceanic convective heat flux and causing crucial changes in the sea-ice thickness and extent (Kurtz and Markus, 2012). Third, the Antarctic snow situation (such as thick snow cover, flooded and refrozen snow types) complicates the heat exchange process between the sea ice and atmosphere, leading to anomalous variations of sea-ice thickness and extent (Giles and others, 2008). As important factors of global climate change, the determination and monitoring of Antarctic sea ice are crucial to the understanding of sea-ice growth and decay, as well as the atmosphere/ocean interactions in the Southern Ocean (Ferrari and others, 2014).

Sea-ice extent can be monitored daily by passive microwave remote sensing with high accuracy; however, there are no accurate observations of basin- or global-scale sea-ice thickness (Kaleschke and others, 2012; Simpkins and others, 2012; Stroeve and others, 2012; Laxon and others, 2013; Peng and others, 2013; Kwok, 2018; Kwok and Kacimi, 2018). The methods of observing sea-ice thickness include surface drillings, ship observations, upward-looking sonar (ULS), and spaceborne and airborne altimeters. Traditional methods such as surface drillings and ship observations can provide measurements of sea-ice thickness with high spatial resolution and cm-level accuracy (Worby and Comiso, 2004; Naoki and others, 2008). However, measurements gathered by man are mostly located in areas that are accessible to people or ships, making measurements of sea-ice thickness that have obvious temporal and spatial limitations and cannot meet the needs of real-time and large-scale monitoring. Therefore, manual measurements are usually used to monitor sea-ice thickness at points of interest or used as in situ data to validate the accuracy of other ice thickness observations. Measuring sea-ice draft with a

sampling rate from seconds to hours, ULS can provide continuous draft observations to study the high-frequency variation in sea-ice thickness (Behrendt and others, 2013, 2015). A submarine ULS can measure the lower surface geometry of sea ice in an area of interest, while a moored ULS can continuously monitor the sea-ice draft and its annual and interannual variations at points of interest. In addition to the difficulty in obtaining large-scale sea-ice draft, ULS measurements are also affected by drift if the sea ice moves freely with currents while the ULS instrument is moored at the ocean bottom (Behrendt and others, 2015).

By calculating the height difference between the snow surface (or sea-ice surface) and sea-water surface or leads (a passage of open water within an expanse of sea ice), an altimeter can obtain the total freeboard of sea ice (or sea-ice freeboard) (Zwally and others, 2008; Ricker and others, 2014). With the density of sea ice and snow as well as snow depth, the sea-ice thickness can be calculated under the assumption of hydrostatic equilibrium. In this study, we define the sea-ice freeboard as the distance from the sea-ice surface to the sea-water surface (or freeboard for short, which is positive when the freeboard is above the sea-water surface and negative when it is below the sea-water surface) and the total freeboard as the sum of sea-ice freeboard plus snow depth. Laser altimeters, i.e., the Ice, Cloud and land Elevation Satellite (ICESat), can be used to extract the total freeboard if snow is present (in most cases when studying the Antarctica sea ice) because the near-infrared laser signal does not penetrate but is reflected by the snow surface (Kwok and others, 2007; Zwally and others, 2008; Kwok and Rothrock, 2009). Although ICESat has the advantages of small footprint and high-accuracy elevation measurements, it is temporarily limited to autumn and spring seasons due to the corrosive degradation of its pump diodes, as well as spatially limited by the presence of clouds. Its successor, ICESat-2, was launched in September of 2018 (Abdalati and others, 2010). ICESat-2 employs a multibeam photon-counting lidar for profiling the surface, providing information on unique characteristics of the retrieved elevations compared to traditional waveform altimetry (Kwok and others, 2019). To best apply its observations to sea-ice research, the precision and accuracy of ICESat-2 still need to be assessed using as much in situ observation data as possible. Radar altimeters, i.e., the Cryosphere Satellite-2 (CryoSat-2), can be used to extract sea-ice freeboard by measuring the distance from the snow/ice interface to the sea-water surface (Laxon and others, 2013; Kurtz and others, 2014). Unlike laser and optics technologies, radar is cloud and snow penetrating. However, studies show that the moisture and layering density of snow may prevent the radar from penetrating to the snow/ice interface, and the large footprint of radar and the roughness of sea ice may also lead to large uncertainties in the retrieval of freeboard (e.g., Ricker and others, 2014). In addition to satellite altimeters, NASA's Operation IceBridge (OIB) mission provides high-accuracy freeboard measurements at areas of interest (Farrell and others, 2011; Kwok and others, 2012). OIB can acquire cloud-free remote-sensing data by flying under clouds and identify leads accurately using its onboard digital mapping system camera. Implemented as an interim programme to fill the gap between ICESat and ICESat-2, OIB allows us to study the interannual behaviour of sea ice and provides an opportunity to better understand the issues associated with the retrieval of sea-ice freeboard and thickness (Kurtz and others, 2013; Xia and Xie, 2018).

Whether using sea-ice draft observed by ULS or freeboard (total freeboard) retrieved by altimeters to calculate sea-ice thickness based on the hypothesis of hydrostatic equilibrium, additional information is needed, such as sea-ice density, snow density and snow depth (Massom and others, 2001). The retrieval uncertainty of sea-ice thickness is dominated by the measurement uncertainties of snow depth (~50%) and freeboard (~40%), as well as small contributions from the density uncertainties of water, sea ice and snow (Giles and others, 2007). The so-called 'Warren climatology', which is based on the comprehensive analysis of snow depth measurements at drift stations and airplane landing areas in the Arctic, provides alternative values for snow depth and density (Warren and others, 1999). However, many have suggested that the Warren climatology may be out-dated and problematic when used in Antarctica (Kurtz and Markus, 2012; Webster and others, 2014).

The premise of using spaceborne or airborne altimeters to retrieve sea-ice thickness is to accurately extract and separate freeboard and snow depth. Field measurements are the most accurate and reliable methods to achieve this goal, but it is difficult to manually acquire freeboard and snow depth synchronized with altimeter observations, or to continuously monitor them at high frequencies in the areas of interest. Due to the accuracy improvement, the GPS is able to monitor displacement with an accuracy at the centimetre or even millimetre level, and it has been widely used in studies of crustal load effects, co/post-seismic deformation, and sea-ice concentration (Larson, 2009; Fu and others, 2015; Semmling and others, 2019). Aoki and others (2002) used GPS observations on sea ice to evaluate the seasonal sea-level variations at Antarctic Syowa Station and found that GPS and BPG techniques show consistency with a RMSE of 0.7 cm. King and Aoki (2003) proposed an approach using a single GPS receiver deployed on floating sea ice to measure ocean tides; the successful application of this approach proves that GPS can be used to observe ocean tides at high latitudes where remote sensing or tide gauge measurements are lacking. Lei and others (2018) applied the same approach to derive the ocean tides at Antarctic Zhongshan Station and found that the RMSE between GPS-derived and BPG-derived tides for the eight major constituents (O_1, K_1, P_1, Q_1, M_2, S_2, N_2, K_2) was better than 4 cm. In addition to the sea-ice motion, GPS can also be used to obtain snow depth around it using the so-called GPS interferometric reflectometry (GPS-IR) technique. For example, Siegfried and others (2017) employed the GPS-IR technique to measure snow accumulation across a 23-station GPS array in West Antarctica, proving that GPS-IR is an effective technique for monitoring snow depth variation.

In this paper, we use a floating GPS deployed on land-fast sea ice to monitor the variations of freeboard and snow depth in Nella Fjord near China's Zhongshan Station. By validating with surface drilling measurements and reanalysis products, our methods are proven to be feasible and reliable for obtaining freeboard and snow depth. The time series of freeboard and snow depth obtained by GPS can be used to supplement our understanding of sea-ice freeboard and snow depth, or to assess the accuracy of sea-ice freeboard measurements from spaceborne or airborne altimeters. The applicability of hydrostatic equilibrium in Nella Fjord is also analysed. The arrangement of this paper is as follows: Section 2 presents the experimental setup and the data used in this study. Section 3 introduces the methodologies used to process GPS observations and estimate the sea-ice freeboard and snow depth as well as Stefan's Law for snow-covered ice. The main results are given in Section 4. Section 5 discusses the accuracy and reliability of our methods as well as the feasibility of the single-point hydrostatic equilibrium hypothesis. A summary is given in Section 6.

2. Experiment

2.1 Layout

Managed by the Polar Research Institute of China, Zhongshan Station is located in the Larsemann Hills near Prydz Bay in East Antarctica. To verify the feasibility of retrieving sea-ice

https://doi.org/10.1017/aog.2020.41 Published online by Cambridge University Press

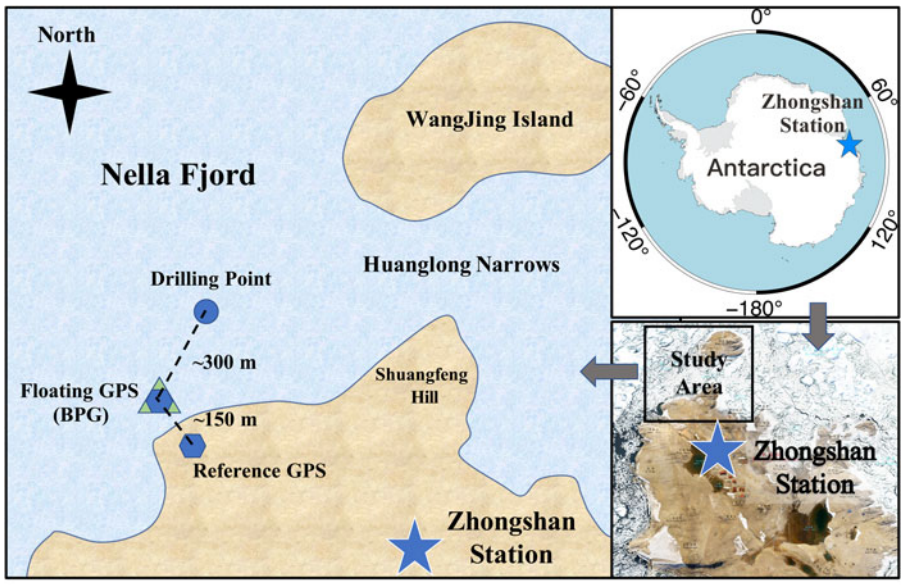

Fig 1. Map of Zhongshan Station and study area, as well as the locations of reference and floating GPS receivers, bottom pressure gauge and drilling points.

freeboard and snow depth using floating GPS, the Chinese 33rd Antarctic Scientific Research team carried out field experiments on land-fast sea ice in Nella Fjord near Zhongshan Station. Figure 1 shows the locations of Zhongshan Station and our study area, as well as the locations of the reference and floating GPS, bottom pressure gauge, and drilling points in the study area. A Leica dual-frequency GPS receiver (floating GPS, photo is shown in Figure S1 in the Supporting Material) was deployed on land-fast sea ice ~100 m away from the coastline and 150 m away from a continuously operational Leica dual-frequency GPS receiver (reference GPS) on the bedrock of Tian-e Ling. To resist the strong wind, we placed the tripod with its legs frozen on the sea ice and keep the height of the GPS antenna ~1 m above the sea-ice surface. To remove the effects of, for example, ocean tides and time-varying dynamic ocean topography on the retrieval of sea-ice freeboard, the floating GPS was deployed on the top of a bottom pressure gauge (BPG), which could accurately observe the total pressure upon it. Combined with the atmospheric pressure observations from a barometer at the Zhongshan Station, we could subtract the atmospheric pressure from BPG observations and then calculate the sea-water depth and its variations. During the observations, we also conducted manual drilling measurements at two points on the sea ice (Zhao and others, 2017). The two drilling points were ~300 metres northeast of the floating GPS, and the distance between the two drilling points was several tens of metres (shown as a single point in Fig. 1). At the drilling points, the snow depth, sea-ice freeboard and thickness were measured. These manual measurements were used to assess the sea-ice freeboard and snow depth derived from the floating GPS.

2.2 Data

The sea-ice motion, including the variations in sea-ice freeboard and sea-water depth, were observed by a floating GPS receiver during sea-ice growth in Nella Fjord near Zhongshan Station. Figure 2 shows the relationship among snow depth h_s, freeboard h_f, total freeboard h_t, sea-ice draft h_d, and sea-ice thickness h_i (left), as well as the schematic diagram of freeboard and snow depth observed by the floating GPS (right). At the beginning of the observation, the height from the GPS antenna to the sea-ice surface (h_1) and the height from the GPS antenna to the waterline (h_r) were measured manually, and the h_1 was measured several times during the observations. Due to bad weather and logistical reasons, the experiment in 2017 consists of two periods: the first period is from day of year (DOY) 235 to 252 (18 d) and the second period is from 286 to 324 (39 d). The values of h_1 measured repeatedly during the experiments only vary on the order of mm, indicating that the freezing and melting on the sea ice upper surface is negligible. This is reasonable because during our observation, there was >10 cm snow cover, which isolated the sea ice from air-ice energy exchange to a great extent.

The BPG deployed beneath the floating GPS could observe the sea-water depth h_w in combination with the atmospheric pressure observation from an onshore barometer (corrected to sea level). The inverse barometer effect influenced both BPG and GPS measurements and was thus ignored. The pressure P at depth h_w in a liquid is represented by the following formula:

$$P = \rho_w g h_w \quad (1)$$

where P is pressure caused by sea water, h_w is the sea-water depth, $\rho_w = 1.028$ g cm^{-3} is the sea-water density when the sea-water temperature is −1.8° and the salinity is 3.5%, and $g = 982.57$ cm s^{-2} is the gravity observed by an high-accuracy absolute gravimeter at the Zhongshan Station after reduction to sea level. The sea-water density is the main source of uncertainty in the computation of sea-water depth. During the observations, we collected several sea-water temperatures and salinity measurements. With different combinations of these variables, the sea-water density ranged from 1027.5 to 1028.5 g cm^{-3}. Thus, the uncertainty caused by density is ~0.1% in our case. The sea-water depth in our study area is ~8 metres, so the absolute accuracy of BPG-observed sea-water depth is ~1 cm. The sea-water depth consists of a constant height h_{msl} from the long-term mean dynamic ocean topography (MDT) to the BPG location (including the height from the long-term MDT to the geoid and the height from the geoid to the sea floor), periodic ocean tides h_{tides} caused by the sun and moon, the time-varying dynamic ocean topography h_{topo} and the high-frequency variation Δh caused by currents and surges. The different locations of the floating GPS, BPG and drilling points would cause systematic deviations in the freeboard time series. We first calculated the absolute accuracy of freeboard estimates with respect to drilling measurements, and then, by using the drilling measurements as reference, we removed the average bias between drilling measurements and freeboard time series for each observation period and focused on verifying the potential of using a floating GPS to monitor the freeboard variations. Periodic ocean tides h_{tides} and dynamic

https://doi.org/10.1017/aog.2020.41 Published online by Cambridge University Press

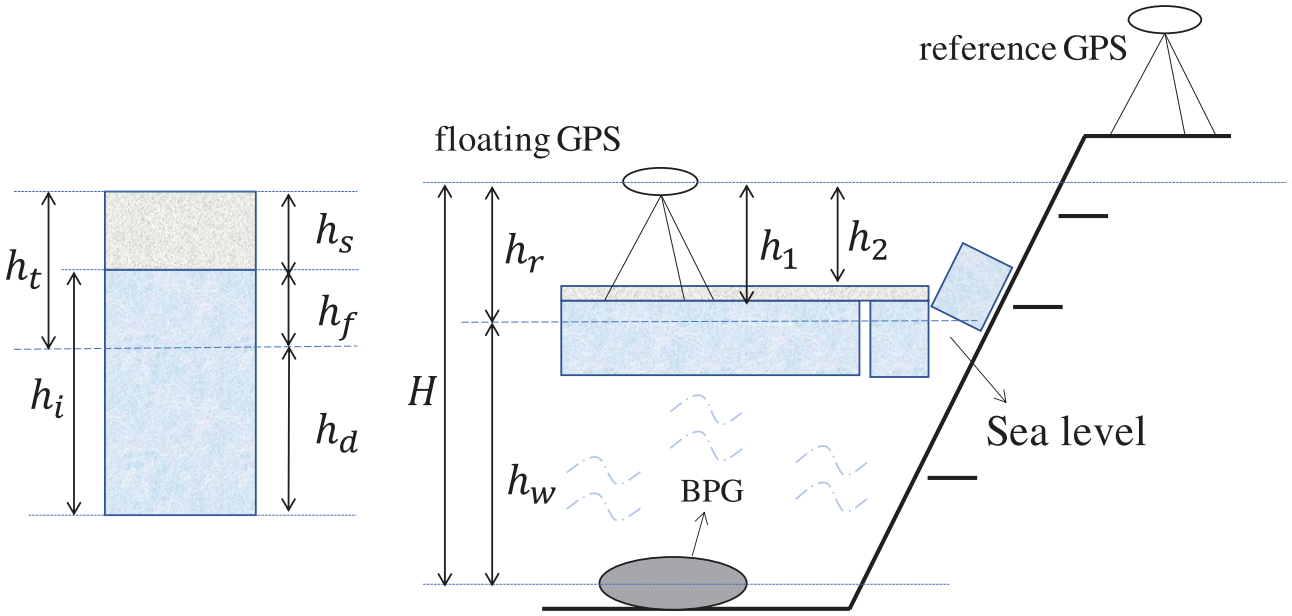

Fig 2. Relationship among snow depth h_s, freeboard h_f, total freeboard h_t, sea-ice draft h_d, and sea-ice thickness h_i (left), as well as the schematic diagram of freeboard and snow depth observed by floating GPS (right).

topography h_{topo} are functions of time and cannot be eliminated by long-term synchronous observation. We studied the effects of using different ocean tide corrections derived from BPG, GPS and global ocean tide models on the accurate retrieval of freeboard. We selected TPXO9 as the representative of the global tide model for the follow-up study (see the accuracy assessment of different ocean tide models in Fig. S2 in Supporting Material) (Dushaw and others, 1997 (update); Lei and others, 2018).

During the growth of sea ice, we also carried out surface drillings at two fixed points (~300 m away from the floating GPS), where snow depth, sea-ice freeboard and thickness are measured (Zhao and others, 2017). The time span of surface drillings is from DOY 101 to 341, and its interval is approximately once a week. The surface drillings were mostly collected at 3:00 p.m. local time, which is 10:00 a.m. UTC time. Snow depth, sea-ice freeboard and thickness were measured each time from tworandomly chosen boreholes and their mean value was used to represent a single measurement. If the difference between the two boreholes was >1 cm for sea-ice freeboard or thickness, we drilled a third (or even fourth) borehole and then discarded the greatest outlier and averaged the others. In some instances, the seawater would flow through the borehole so that the sea ice was under the sea water, producing negative freeboard. In these cases, we waited until the upward-flowing sea water was still, measured the water depth above the sea-ice surface and assigned a negative value to these freeboard measurements. The total surface drillings included 33 and 31 sets of measurements at drilling point 1 and drilling point 2, respectively (Table 1). The accuracy of sea-ice freeboard and thickness measurements was within 1 cm, while the accuracy of snow depth measurements was ~3 cm. Considering the sparsity of drilling measurements, we combined the two drilling measurements into one time series and used it to assess the results of GPS-derived sea-ice freeboard and snow depth.

Table 1. Snow depth, sea-ice freeboard and thickness measured by surface drillings (cm)

Drilling Point 1				Drilling Point 2			
DOY	Snow depth	Freeboard height	Sea-ice thickness	DOY	Snow depth	Freeboard height	Sea-ice thickness
118	1	4	52	101	0	4	43
124	0	3	49	111	3	3	52
130	0	5	58	125	0	6	56
138	1	6	67	130	0	5	60
145	2	7	71	137	0	6	68
152	1	7	69	144	4	6	66
158	1	9	73	151	2	6	68
166	0	10	87	157	1	6	72
173	2	11	98	165	0	10	86
180	8	8	105	178	12	11	102
187	21	15	112	185	21	8	105
193	19	22	120	192	23	8	107
201	55	5	113	206	30	4	115
208	20	5	115	214	23	4	115
215	22	2	114	228	35	0	120
219	18	6	117	235	40	0	116
226	45	6	125	242	40	−3	118
235	35	0	116	249	38	−2	122
240	41	−3	112	256	34	6	127
248	40	−3	130	263	35	2	130
255	43	2	134	270	40	2	126
262	47	−4	133	278	35	3	133
269	48	3	132	284	30	0	135
276	42	3	140	292	33	7	142
283	46	−1	137	298	30	5	140
290	42	4	141	305	28	9	144
297	37	6	145	312	30	6	140
304	35	9	146	319	30	5	139
311	33	7	145	326	33	3	130
318	35	4	141	333	28	7	142
326	40	−1	138	341	43	2	139
333	52	−3	137				
341	46	0	142				

3. Methodologies

3.1 GPS data processing

The TRACK module from GAMIT/GLOBK (Herring and others, 2010) and PPP-AR from the PRIDE group of Wuhan University (Geng and others, 2019) were used to resolve the relative positioning and the precise point positioning (PPP) solutions of the vertical displacements of floating GPS, respectively. Relative positioning can eliminate or mitigate most positioning errors, enabling the relative time series to achieve mm-level accuracy. However, relative positioning undergoes significant precision

https://doi.org/10.1017/aog.2020.41 Published online by Cambridge University Press

degradation as baseline distances increase, whereas PPP does not. In this study, we used the relative solutions to show the best performance achieved when using floating GPS to monitor sea-ice motion and the corresponding sea-ice freeboard variations, and we used the PPP solutions to test the applicability of using floating GPS to monitor freeboard variations in the locations much farther from shore.

The success of relative processing (TRACK) depends on the separations of the moving station and the reference station; as distance increases, the differences in atmospheric delay also increase. TRACK uses the Melbourne-Wubbena combination to estimate the wide-lane ambiguity first and then determine L1 and L2 cycles separately (Herring and others, 2010). The antenna phase centre offset (PCO) and variation (PCV) of ground antennas are modelled using the azimuth and elevation model (AZEL) while the PCO and PCV of satellite antennas are modelled using the elevation-dependent model (ELEV). The IERS2003 model is used as solid Earth tide corrections while the relative ocean tide loading displacements (OTL) over our short baseline were mostly cancelled; thus, we did not apply OTL corrections. TRACK has the ability to include, for example, IONEX files to help with the ionospheric delay on long baselines. As the distance between the reference GPS in Tian-e Ling and the floating GPS was only ~150 m, the relative processing strategy of TRACK could eliminate most positioning errors such as atmospheric delays. Therefore, we did not further correct or estimate these values but, rather, used the 'zero' mode to calculate the displacement of the floating GPS epoch by epoch relative to the reference GPS for L1 and L2 frequencies separately. Not needing to estimate tropospheric parameters or combine ionosphere-free observation for short baselines gives relative positioning (TRACK) higher precision compared with PPP. The average RMSE for all epochs in the TRACK solutions was ~4 mm for both L1 and L2, and we discarded the outliers with RMSE >10 mm (<1% of observations were discarded). We also compared the results between L1 and L2 and found their consistency to be good, with standard deviation <1 cm. To make these results compatible with the GPS-IR results, we used L1 solutions as the relative time series.

Retrieving the integer property of single-station ambiguities in PPP is more difficult, which makes the PPP accuracy worse than that of the relative positioning. The processing strategy of PPP-AR is as follows: the vertical coordinate is calculated using the kinematic processing mode with a 30 s time interval; the elevation cut-off is set to 10° to mitigate the potential multipath. The antenna phase centre offset (PCO) and variation (PCV) are corrected using the IGS14 atx file. The undifferentiated ionospheric-free pseudorange and phase combination observable are used to remove the first-order ionospheric delays, and the impacts of higher-order delays are ignored. Notably, the ionospheric-free combination would amplify noise ~threefold compared with those using L1 or L2 independently for baselines less than several kilometres (Schaffrin and Bock, 1988). The tropospheric delays are first corrected with the Saastamonion model for a priori wet and dry delays, and then the residual zenith delays are estimated as random-walk parameters for each epoch with the GMF mapping function. Solid Earth tides of IERS2003 and ocean tide loading calculated using TPXO9 are used as tidal corrections. The fiducial satellite orbit and clock information is obtained from IGS final SP3 precise ephemeris in the IGS14 reference frame, and the receiver clocks are estimated as white-noise-like parameters. Other settings and parameters were default. The single-station ambiguity resolution makes use of the phase clock/bias products released by the PRIDE lab (ftp://igs.gnsswhu.cn/pub/) to recover its integer nature and then carry out integer ambiguity resolution. To assess the PPP accuracy, we calculated the difference in time series between PPP-AR solutions and TRACK L1 solutions; the standard deviation of the difference in time series was ~2.5 cm.

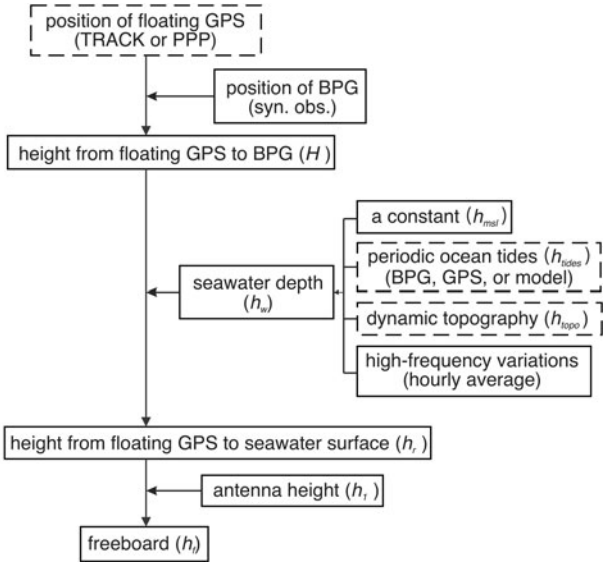

Fig 3. The processing scheme to retrieve the sea-ice freeboard. The factors in the dashed boxes were further analysed by using different combinations of them.

After GPS data processing, we obtained two types of solutions. The PPP kinematic solutions were in the IGS14 reference frame, while TRACK solutions were based on the onshore reference GPS. We also used the PPP-AR to calculate the daily coordinates of reference GPS and used the mean coordinates during the two experimental periods to transform the TRACK relative solutions into the IGS14 reference frame.

3.2 Sea-ice freeboard

The sea water in Nella Fjord begins to freeze in early March. The new land-fast sea-ice gains thickness until December and rapidly melts in a few months. In the following February, the sea ice disappears, and a new cycle begins again in March. During its growth, the vertical motion of sea ice was observed by a floating GPS deployed on it. Figure 3 illustrates the processing scheme used to retrieve the sea-ice freeboard.

The height H from the floating GPS antenna to the sea floor (BPG) mainly consists of two parts:

$$H = h_{\mathrm{w}} + h_{\mathrm{r}} \tag{2}$$

$$\begin{aligned} h_{\mathrm{w}} &= h_{\mathrm{msl}} + h_{\mathrm{tides}} + h_{\mathrm{topo}} + \Delta h \\ h_{\mathrm{r}} &= h_1 + h_{\mathrm{f}} \end{aligned} \tag{3}$$

where h_{w} is the sea-water depth, including the height from long-term mean ocean topography to the BPG h_{msl}, ocean tides h_{tides}, time-varying dynamic topography h_{topo} and high-frequency variation Δh caused by currents and surges, etc.; h_{r} is the distance from the GPS antenna to the sea-water surface, including freeboard h_{f} and the distance from the GPS antenna to the sea-ice surface h_1. By manually measuring the sea-ice freeboard h_{f}, antenna height h_1, as well as the h_{w} observed by BPG at the time t_0, we could link the floating GPS displacement to the sea-ice motion (Huang and Zhang, 2012). To eliminate or weaken the influence of high-frequency signals (Δh) as well as the potential multipath effect on the GPS positioning time series, the hourly median of sea-ice freeboard was calculated. The constant h_{msl} can be obtained from previous simultaneous observations, while

https://doi.org/10.1017/aog.2020.41 Published online by Cambridge University Press

the variations in the hourly GPS displacement at any time t with respect to t_0 are only related to ocean tides h_{tides}, dynamic topography h_{topo}, and the sea-ice freeboard h_f. BPG can provide observations of ocean tides h_{tides}, dynamic topography h_{topo} with respect to t_0. Alternatively, periodic ocean tides can be calculated from the floating GPS or global tidal models. The high-accuracy time-varying dynamic topography h_{topo} is difficult to obtain in the Southern Ocean, especially for those areas where sea-ice exists (King and others, 2009; Griesel and others, 2012). In Section 5, we will discuss the effects of using different GPS processing data, different ocean tide corrections, and whether or not dynamic topography is considered on the accurate retrieval of freeboard (factors in dashed boxes in Fig. 3). For the freeboard h_r, if the melting and freezing of sea ice on the upper surface can be neglected compared with those of the lower surface (confirmed by manual measurements), that is, the distance from the GPS antenna to the sea-ice surface (h_1) is fixed and measured, then the freeboard h_f can be obtained from the GPS-observed vertical displacement.

3.3 Inversion of snow depth

GPS-IR is a method for estimating environmental parameters around a (nominally multipath suppressed) geodetic-quality GPS antenna without the need for a designed or rotated antenna to measure reflection signals (Roesler and Larson, 2018). GPS-IR has been demonstrated and validated for measuring surface soil moisture, tides, vegetation water content and snow depth (e.g., Larson, 2016; Siegfried and others, 2017; Roesler and Larson, 2018). To some extent, GPS-IR studies are based on the analysis of signal-to-noise ratio (SNR) patterns created by the interference of direct and reflected signals, which can be modelled as follows (Axelrad and others, 2005):

$$\mathrm{SNR}(e) = A(e)\sin\left(\frac{4\pi H_R}{\lambda}\sin e + \phi\right) \tag{4}$$

where $A(e)$ is the SNR amplitude, H_R is the reflector height that represents the vertical distance from the GPS antenna to the horizontal reflecting surface, e is the elevation angle of the GPS satellite with respect to the horizon, λ is the wavelength of the GPS signal and ϕ is the initial phase. Based on a simple assumption that all other reflected conditions of snow for GPS signals remain unchanged (in other words, the amplitude A and initial phase ϕ are kept fixed), we can estimate the variation in reflector height H_R by the changes in the so-called multipath frequency $2H_R/\lambda$. In our study, H_R is the distance from the antenna to the snow surface, which is the same as h_2 as shown in Figure 2. Considering that the distance from the antenna to the sea-ice surface remains fixed, the snow depth h_s can be calculated as follows:

$$h_s = h_1 - h_2 \tag{5}$$

3.4 Stefan's law for snow-covered ice

There were only 15 manual measurements of sea-ice thickness during 57 d of floating GPS observations. To fully analyse the relationship among freeboard, snow depth, and sea-ice thickness for all 57 d, we modelled the thermodynamic growth of sea ice based on Stefan's assumption that the heat loss during the freezing process is directed upward and is completely balanced by the latent heat of fusion of the sea ice (Allison, 1981; Behrendt and others, 2015). The energy balance at the ice/ocean interface determines the growth rate of the sea ice $\mathrm{d}H/\mathrm{d}t$ (Petrich and Eicken, 2010):

$$\rho_i L_i \frac{\mathrm{d}h_i}{\mathrm{d}t} = F_c - F_w \tag{6}$$

where ρ_i is the density of sea ice, L_i is the latent heat of fusion of the sea ice, F_c is the conductive heat flux through the sea ice, and F_w is the oceanic heat flux from below. In the case of snow cover (of thickness h_s) on top of the sea ice (of thickness h_i), the conductive heat flux F_c can be expressed by Fourier's law of heat conduction (Behrendt and others, 2015):

$$F_c = \frac{T_w - T_0}{(h_i/\lambda_i) + (h_s/\lambda_s)} \tag{7}$$

where T_w and T_0 are the sea-water temperatures and snow surface temperature, respectively. λ_i and λ_s are the thermal conductivity of sea ice and snow, respectively. Since the snow surface temperature T_0 is difficult to measure and thus usually not known, an alternative is to use the air surface temperature. The net heat flux between the air and the snow surface F_a can then be parameterized by the following linear approximation (Leppäranta, 1993):

$$F_a = \kappa(T_0 - T_a) \tag{8}$$

The air surface temperature T_a is taken from the automatic weather station at Zhongshan Station. As a function of wind speed, snow insulation, humidity, and so on, the effective heat transfer coefficient κ can be determined by measuring the growth of sea ice under different meteorological conditions. By assuming $F_c = F_a$ (Leppäranta, 1993; Behrendt and others, 2015), Eqn (3) can then be written as follows:

$$\rho_i L_i \frac{\mathrm{d}h_i}{\mathrm{d}t} = \frac{T_w - T_a}{(1/\kappa) + (h_i/\lambda_i) + (h_s/\lambda_s)} - F_w \tag{9}$$

The daily growth rate $\mathrm{d}h_i/\mathrm{d}t$ of the sea-ice thickness can be obtained by solving Eqn (9), and then, the sea-ice thickness h_i can be obtained.

4. Results

4.1 Sea-ice freeboard

According to the above sections, we obtained two sets of GPS vertical time series (relative solution from TRACK and PPP solution from PPP-AR), three sets of ocean tide corrections (BPG, GPS and TPXO9) and the time-varying dynamic topography correction from BPG (BPG observations minus BPG-tides and mean depth). Six solutions of hourly freeboard time series can be obtained by combining the above datasets: solution 1: TRACK + BPG tide + dynamic topography; solution 2: PPP + BPG tide + dynamic topography; solution 3: TRACK + GPS tide + dynamic topography; solution 4: TRACK + TPXO9 tide + dynamic topography; solution 5: TRACK + BPG tide; and solution 6: PPP + GPS tide. Since the freeboard beneath the floating GPS at the beginning of observations was measured, we align all six solutions to this value. Figure 4 shows the six solutions of freeboard time series. The freeboard time series of solution 1 is relatively stable, which indicates that the floating GPS can obtain high-precision results after removing the effects of ocean tides and dynamic topography. Solution 1 also shows that the freeboard is time varying. For 1 d or even 1 hour, the range between maximum and minimum freeboard is on the order of cm. Therefore, using in situ measurements to evaluate the altimeter-retrieved freeboard may contain errors caused by

https://doi.org/10.1017/aog.2020.41 Published online by Cambridge University Press

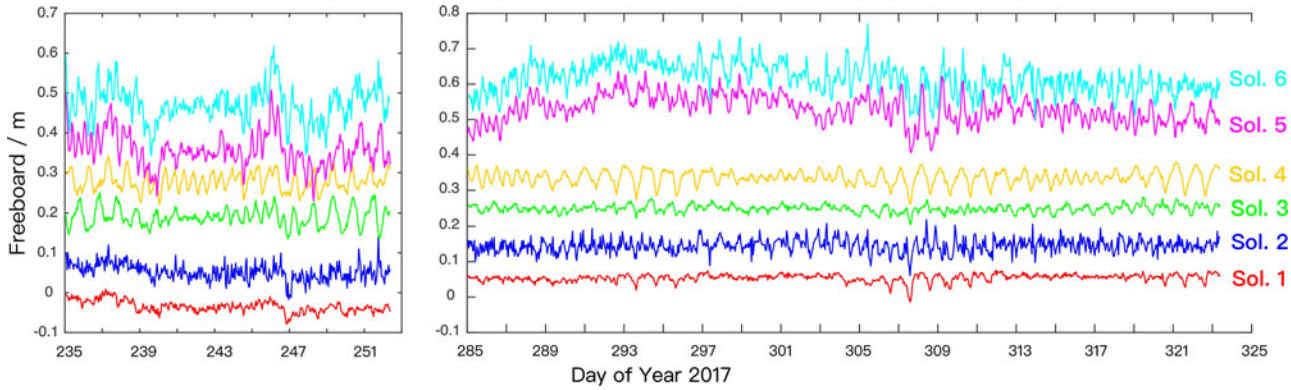

Fig 4. Six solutions of freeboard time series. solution 1: TRACK + BPG tide + dynamic topography; solution 2: PPP + BPG tide + dynamic topography; solution 3: TRACK + GPS tide + dynamic topography; solution 4: TRACK + TPXO9 tide + dynamic topography; solution 5: TRACK + BPG tide; and solution 6: PPP + GPS tide. Accumulated offsets of 0.1 m are added for the respective solutions to improve visibility (an offset of 0.2 m is added for solutions 5 and 6 in the first period due to their sharp decrease at DOY 235 caused by time-varying dynamic topography).

asynchronous time. The 24-hour continuous floating GPS deployed on the ground track of altimeters not only can realize synchronous observation but also monitor the real-time changes in freeboard time series. By comparing solutions 1 and 2, we can see the effect of different GPS processing strategies on the accurate retrieval of freeboard. By relative positioning with the onshore GPS, the TRACK solution can eliminate or reduce the influence of model residuals, so the freeboard time series of solution 1 is relatively stable. Due to the inadequate removal of positioning errors caused by the undifferentiated satellite position and clock errors, atmospheric refraction and so on, the time series observed by PPP-AR is noisier than that observed by TRACK. Comparing solutions 1, 3 and 4, we can see the effects of different ocean tide corrections on the accurate retrieval of freeboard. There are diurnal and semi-diurnal mis-model signals left in the freeboard time series, especially for solution 4, which uses the TPXO9 model value as its tide correction; as a result, the residual tidal signal is more obvious than that of solution 3, which uses GPS-derived tide correction. This finding is consistent with the accuracy analysis in Figure S2 in the Supporting Material, which shows that the root sum squares for the eight major constitutes (O_1, K_1, P_1, Q_1, M_2, S_2, N_2, K_2) are 5.6 cm and 1.3 cm for TPXO9 and GPS-tide, respectively. By comparing solutions 1 and 5, we can see the effect of time-varying dynamic topography, caused by ocean circulation and sea-water temperature and salinity, on the accurate retrieval of freeboard. Taking DOY 235 and 239 as examples, the effect of dynamic topography may reach decimetre level and cause an offset that influences the subsequent freeboard estimates; therefore, dynamic topography is one of the main error sources in freeboard estimates. This is also the reason why the lowest-point scheme is used to remove the effect of dynamic topography when retrieving freeboard using altimeters (Kwok and others, 2007; Xia and Xie, 2018). Compared with the dynamic topography, the effect of different ocean tide corrections on freeboard is relatively small, with a magnitude of several centimetres. Solution 6 shows the freeboard time series using standalone floating GPS, it is the noisiest time series among all solutions, with apparent features caused by the time-varying dynamic topography.

4.2 Snow depth

The snow depth on the sea-ice upper surface affects the freeboard and sea-ice thickness, as well as the heat exchange between sea ice and atmosphere. GPS-IR uses the SNR data, which reflects the interference effect between the direct incident signal and the reflected (multipath) signal, to invert physical parameters through the variation in amplitude, frequency and phase. We use L1-frequency SNR recorded by floating GPS to invert snow depth. The higher the elevation angle is, the closer the reflector is to the GPS antenna, and thus the smaller is the reflector area. Figures 5a and b show the characteristics of SNR for satellite #5 at DOY 236 as a function of elevation and time, respectively. There is an apparent quasi-period feature for the SNR data with periods varying from 10 to 20 min, especially when the elevation is below 30°. We used this feature to invert the reflection height from the GPS antenna to the reflector according to Eqn (4). According to Roesler and Larson (2018), we chose the SNR data with an elevation range from 5 to 30° and used the Lomb Scargle Periodogram (LSP) to extract SNR spectral content and then express its frequencies in terms of reflection height (Fig. 5c). We calculate the difference between the height from the GPS antenna to the sea-ice surface (h_1) and the reflection heights to present the snow depth. Due to the roughness of the snow surface and the nonhorizontal reflected signals, anomalous inversions of snow depth may appear. During the observation, the snow depth in the experimental area is <50 cm, so the inversion results of the snow depth <0 cm and > 60 cm are taken as outliers (<10%) and thus removed. The snow depth in the Nella Fjord has a complex spatial and temporal distribution under the combined influence of snowfall and drifting, and the standard deviation of all snow depth estimates in a day is ~5 cm; therefore, it is difficult to determine the real-time variation in snow depth. Thus, we use the median to present the daily snow depth.

It should be noted that the quasi-period characteristic of SNR (Fig. 5b) may affect the GPS-observed sea-ice motion time series and the corresponding freeboard time series. Figure 5d shows the power spectral density of TRACK and PPP solutions. In addition to the apparent diurnal and semi-diurnal signals, there are peaks at the periods from 10 to 20 min, which are related to the multipath effect. We used a linear plus sine function to fit the corresponding amplitudes for these peaks and found that there were no significant periods (only ~1–2 mm amplitudes with varying periods). Additionally, the hourly median freeboard estimates could suppress the potential multipath and other high-frequency effects to some extent.

Figure 6 shows the daily snow depth inverted by GPS-IR as well as the manual measurements and the corresponding daily precipitation and wind speed. The snow depth inverted using GPS-IR is quite different from that measured manually. For the first observation period, the snow depth obtained by GPS-IR is ~20 cm, while the snow depth measured manually at the drilling points is ~40 cm. For the second observation period, the snow depth inverted by GPS-IR is ~20 cm in the beginning and

https://doi.org/10.1017/aog.2020.41 Published online by Cambridge University Press

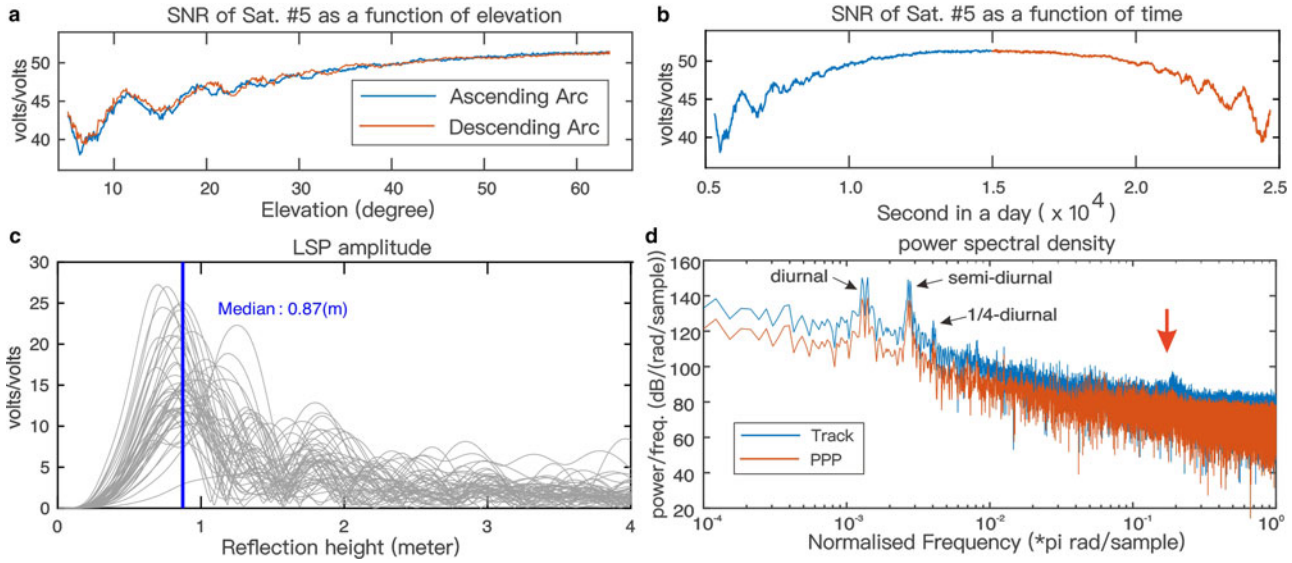

Fig 5. (a) The characteristics of SNR for satellite #5 at DOY 236 as a function of elevation. (b) The same SNR but as a function of time. There is a quasi-period feature for the SNR data, with periods varying from 10 to 20 min. (c) The LSP results of all SNR data for all satellites at DOY 236; the median of reflection height is 0.87 m. (d) PSD for the TRACK and PPP solutions (an offset of −10 dB is added for PPP result for visibility); in addition to the apparent diurnal and semi-diurnal signals, peaks are also found at the periods from 10 to 20 min, which are related to the multipath (SNR) effect.

increase to >30 cm at DOY 307 due to precipitation (snowfall). However, the snow depth of the two drilling points showed a downward trend, and there was also ∼10 cm difference between these two points. These results indicate that, at least in our study area, there are obvious regional (re)distribution characteristics of snow depth. Precipitation shows that three obvious precipitation events occurred during the observation. The snow depth of the GPS-IR inversion increased during these three precipitation events, which indicates that GPS-IR could monitor changes in snow depth to some extent. In contrast, the measurements at the drilling points do not observe two precipitation events, except for the first precipitation event. In addition to the large difference in the spatial distribution of snow depth and the sparse interval between manual drilling measurements, there are also local effects at the drilling points. During our experiment, we found that the snow overaccumulated at drilling points, where the snow depth was usually several or tens of centimetres higher than that in other places. Because we lack the in situ snow depth measurements around the floating GPS for further validation, we still use the snow depth estimates inverted from GPS-IR in the subsequent analysis due to their successful capture of all three precipitation events. In addition, there is no obvious proportional relationship between the precipitation and the snow depth inverted by GPS-IR in the three precipitation events. The possible reason is that the wind affects the spatial distribution of snow depth. Based on the wind speed in Figure 6, strong winds often occur in our study area. During the three precipitation events, the wind speed often exceeds 10 m s^{-1}. Continuous strong winds may cause snow to dramatically redistribute in space. A deep knowledge of snow depth changes caused by precipitation and blowing snow is the basis for the understanding of the mass balance of sea-ice surfaces, which requires in-depth study of the relationship between precipitation, snow depth, wind speed and direction; however, this is beyond the scope of this study.

5. Discussion

5.1 Freeboard validation with respect to drilling measurements

The surface drilling measurements were collected at ∼3:00 p.m. local time, which is 10:00 a.m. UTC time. To mitigate the influence of different observation times on the comparison between GPS-derived freeboard and manual drillings, we calculated the maximum, minimum and median of freeboard obtained by floating GPS from 9:00 to 11:00 a.m. UTC. A total of 15 surface drilling measurements were taken during the experiment. Figure 7 shows the comparison between the GPS-observed freeboard and manual drilling measurements for the six solutions and their RMSEs in the brackets. The high-precision solution 1 (TRACK + BPG tide + dynamic topography) shows the greatest consistency with the surface drilling measurements. Considering the variation of freeboard during the observation hours, almost all of the surface drilling measurements fall in the range of the floating GPS-derived freeboard, with an RMSE of only 1.5 cm. When we use PPP instead of relative processing, the noise in the positioning slightly degrades the freeboard accuracy, and the RMSE of solution 2 is 1.9 cm. If there are no accurate tide observations but GPS-tides or model values are used, cm-level error may be introduced in the freeboard solutions. It should be noted that our drilling measurements were collected at almost the same time every day, which could mitigate the effect of periodic tide on freeboard accuracy to some extent. If drilling measurements are randomly collected at any time, the effect of tides is expected to cause greater errors in freeboard estimates. The time-varying dynamic topography is the main error source that contaminates freeboard estimates. Solution 5 shows that dynamic topography causes an apparent offset in the freeboard estimates. For the first period, all freeboard estimates of solution 5 are much lower than the drilling measurements and even other solutions that consider the dynamic topography, while for the second period, the freeboard estimates of solution 5 are higher than those of other solutions. Similar results can be found for the solution 6. In addition to the influence of time-varying dynamic topography, the position accuracy of the first epoch also influences the potential bias in the freeboard estimates, as do the different locations of the floating GPS, BPG and drilling points. By using the drilling measurements as reference, we remove the average bias between drilling measurements and each freeboard estimates for each observation periods; this allows us to evaluate the precision of using floating GPS to monitor the freeboard variations.

Figure 8 shows the comparison between the GPS-observed freeboard and drilling measurements for the six solutions after

https://doi.org/10.1017/aog.2020.41 Published online by Cambridge University Press

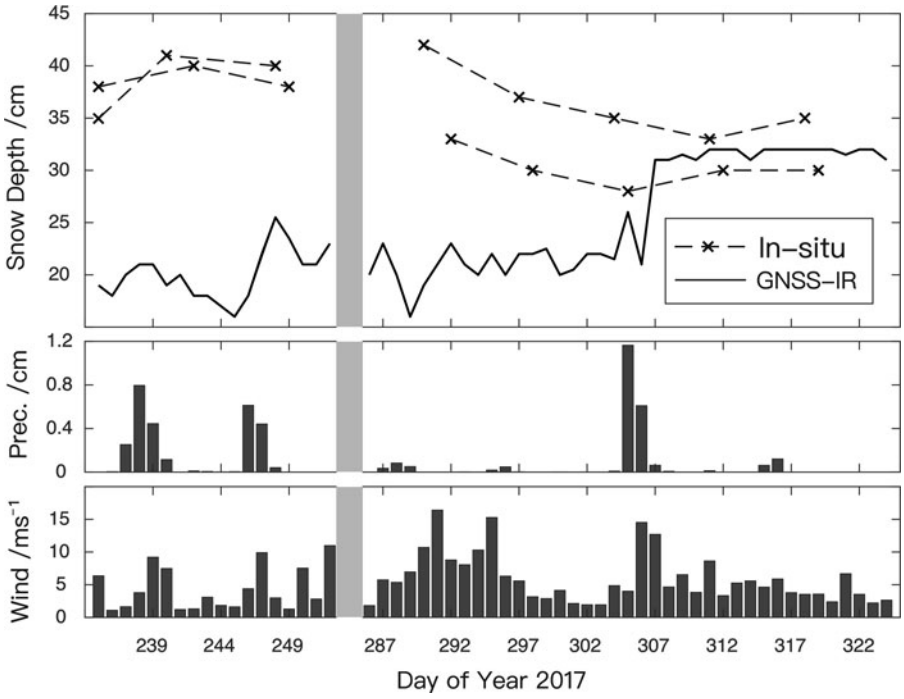

Fig 6. Snow depth inverted using GPS-IR and measured manually, and the corresponding daily precipitation and wind speed.

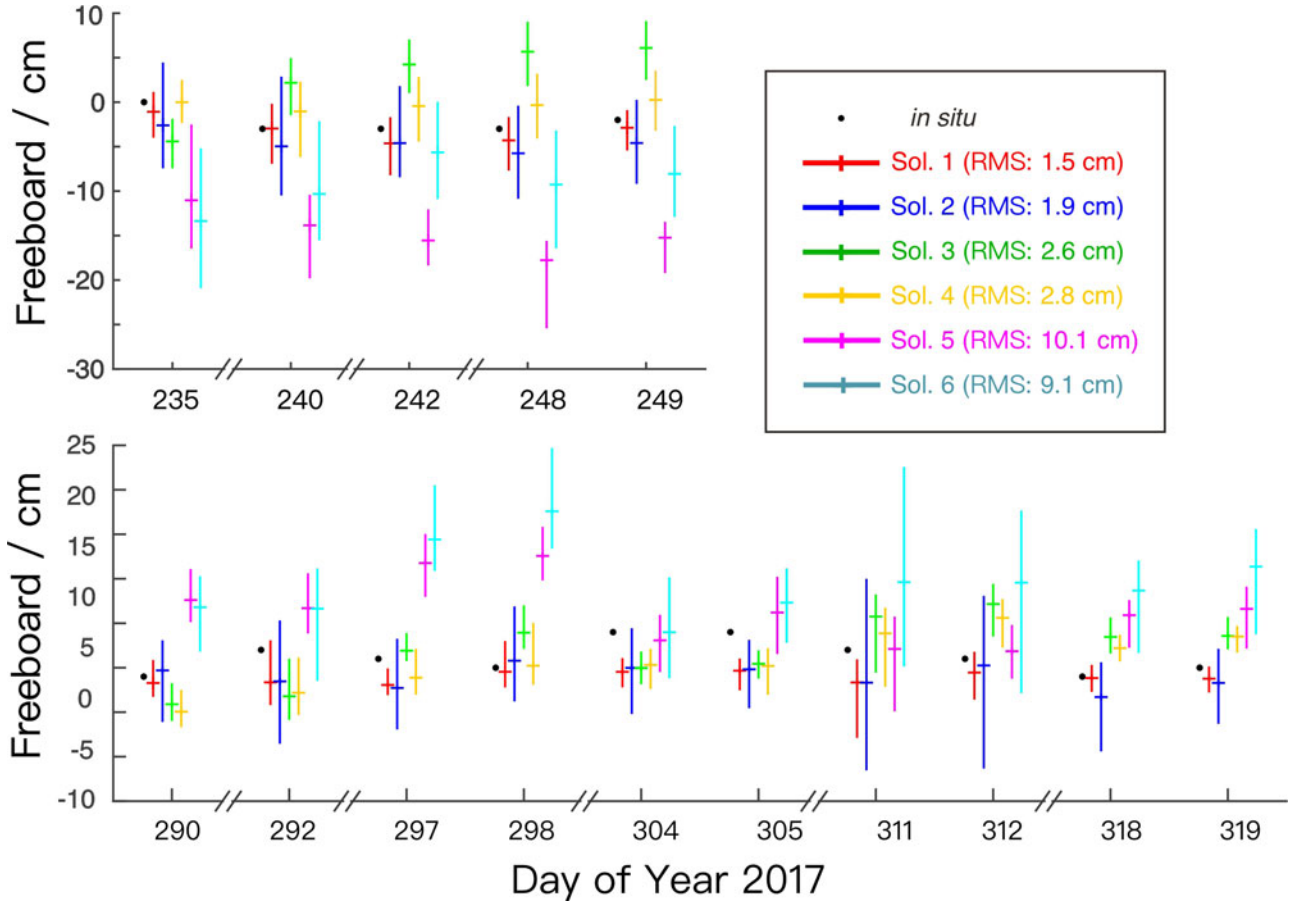

Fig 7. Comparison between the GPS-derived freeboard and manual drilling measurements. The six solutions are the same as in Figure 4. RMSEs in the brackets show the absolute accuracy.

biases are removed for the two periods, with their RMSEs and BIASs in the brackets. The results show that solution 1 (TRACK + BPG tide + dynamic topography) has the best capability for monitoring freeboard variations, with an RMSE of 1.3 cm, which is nearly equal to that of the manual surface drillings (Zhao and others, 2017). Solution 2 (using PPP instead of TRACK) shows the second-best performance, with an RMSE of 1.4 cm, consistent with the absolute assessment results and indicating that using a different processing strategy will only introduce mm-level uncertainty. The relative RMSEs of solutions 3 and 4

https://doi.org/10.1017/aog.2020.41 Published online by Cambridge University Press

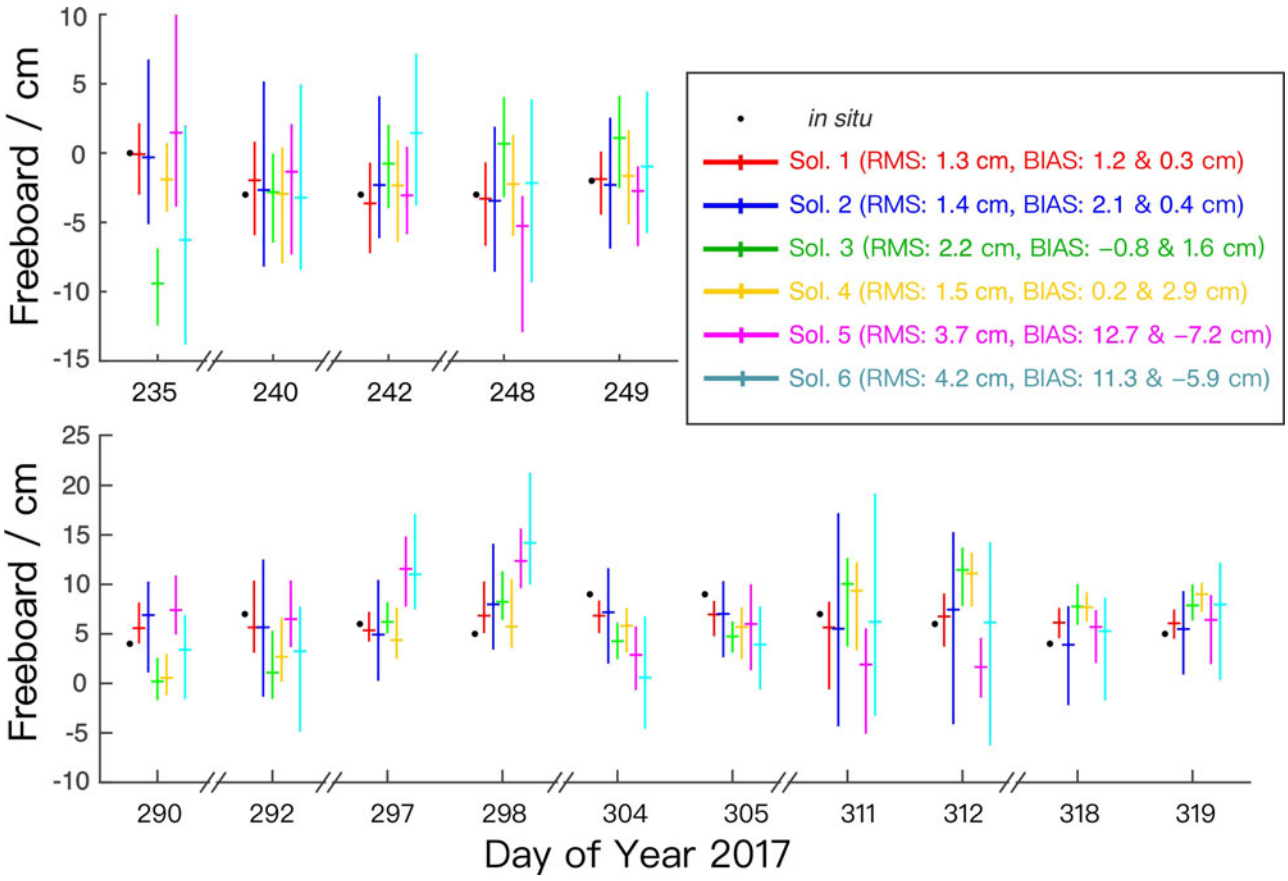

Fig 8. The same as Figure 7 but with bias removed for six solutions. We use the drilling measurements as the reference to calculate and remove the mean bias with each freeboard solution for two periods separately. BIASs in the brackets show the removed bias for two periods, and RMSE shows the respective precision level.

are also improved by removing bias, from 2.6 and 2.8 cm to 2.2 and 1.5 cm, respectively. The most impressive improvements are found for solutions 5 and 6, from 10.1 and 9.1 cm to 3.7 and 4.2 cm, respectively. Generally, in the case of providing accurate time-varying dynamic topography and ocean tides, the floating GPS can observe and monitor freeboard with a precision of better than 2 cm. When the dynamic topography is not available and the ocean tides are less accurate, the precision of ~5 cm freeboard derived from floating GPS is still better than the results with a dm-level accuracy from altimeters. The freeboard time series obtained by floating GPS has the ability to evaluate and verify the accuracy of altimeter-observed freeboard and to supplement our understanding of the time-varying Antarctic sea-ice freeboard.

It should be noted that the bias caused by positioning error in the first epoch and the different locations between drilling points and floating GPS can be removed using this bias-removal method; however, there is still a remaining effect of dynamic topography because of its time-varying feature. Due to the lack of accurate models and/or in situ observations at the Southern Ocean, the dynamic topography is one of the main sources that hinder accurate freeboard retrieval. Additionally, from our analysis, only the hourly freeboard variations are calculated and validated with the weekly drilling measurements. It is currently impossible to further study and analyse the hourly freeboard accuracy and variations. The lack of hour- or even minute-resolution freeboard measurement is one of the reasons we carried out this experiment, and we are considering and devising our next experiment to collect freeboard measurements at higher time resolutions to assess our GPS-observed hourly freeboard estimates and study the effect of, for example, (sub-)daily ocean tides on the freeboard variations. Furthermore, negative freeboards appear in the first period of observations in both the floating GPS (solution 1 as an example) and drilling measurements. For Antarctic sea ice, the existence of the negative freeboard is not only due to the load of snow on it but also due to the dynamic deformation of sea ice caused by factors such as crushing and bending. We will further discuss the applicability of single-point hydrostatic equilibrium hypothesis in the following sections.

5.2 Sea-ice thickness simulation

To fully analyse the relationship among freeboard, snow depth, and sea-ice thickness for all 57 d, the thermodynamic growth of sea ice based on Stefan's law is calculated using Eqn (9). During the period of sea-ice growth, the temperature of sea water is near the freezing point, so we set T_w to −1.8°C. The surface air temperature T_a is taken from the real-time record of the automatic weather station at Zhongshan Station. The sea-ice density is set to 0.92 g cm^{-3}, the latent heat of fusion of sea ice L_i is set to 334 j g^{-1}, and the heat conductivity of sea ice is set to 2.2 W m^{-1} K^{-1} (Behrendt and others, 2015). The influence of snow is mainly reflected in the ratio of snow depth to snow thermal conductivity h_s/λ_s and the air-snow effective heat transfer coefficient κ. All these snow parameters are strongly correlated with the snow types. For snow depth, to minimize the possible snow overaccumulation at drilling points, we first perform a curve fitting to all the manual measurements of snow depth and then multiply the fitting depth $\overline{h_s}$ by a factor α to present the real snow depth; in other words, we rewrite h_s/λ_s into $\alpha\overline{h_s}/\lambda_s$, where we consider $\beta = \alpha/\lambda_s$ to be the snow coefficient. By varying the value of β to obtain the best fitting curve for the

https://doi.org/10.1017/aog.2020.41 Published online by Cambridge University Press

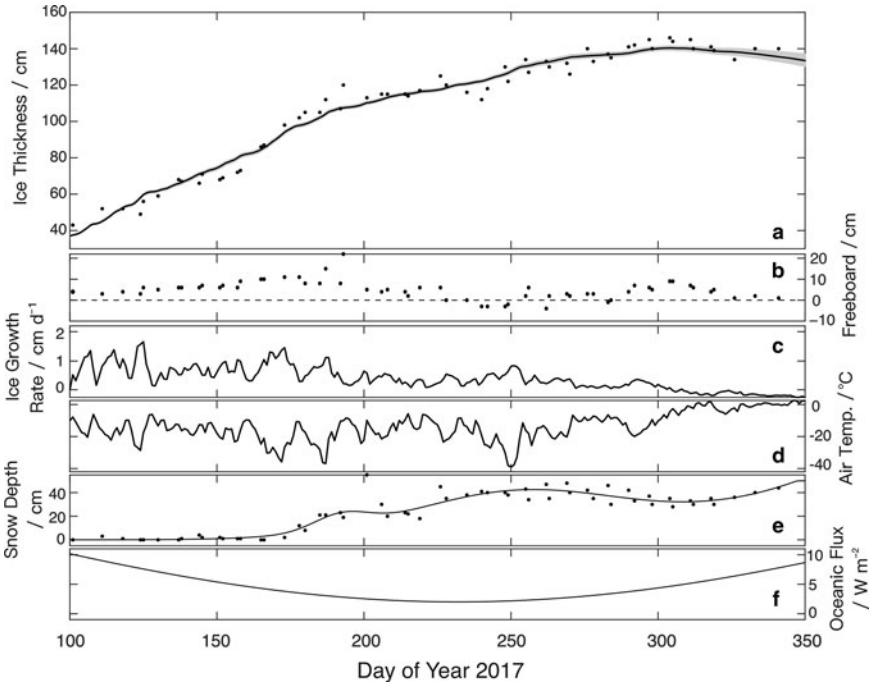

Fig 9. (a) The sea-ice thickness curve based on Stefan's law; solid lines are our simulations, in which the black line is calculated based on the optimal parameter combination and grey lines are the result set of the best 1% parameter combination; the black dots are the drilling measurements of sea-ice thickness. (b) Growth rate of sea-ice thickness. (c) Air surface temperature. (d) Measured snow depth and fitting curve. (e) Default oceanic heat flux.

manual measurements of surface drillings and with the given possible range of snow thermal conductivity λ_s in [0.07 0.45] W m^{-1} K^{-1} (Sturm and others, 1998), we obtained a reasonable snow depth value. Petrich and Eicken (2010) assumed that the air-snow effective heat transfer coefficient κ is in the range of [10 45] W m^{-2} K^{-1} based on measurements of sea-ice growth under different environmental conditions, while Behrendt and others (2015) modelled the value of κ as ~60 W m^{-2} K^{-1} based on the simulation of the ULS data. Based on the abovementioned literature, we set the range of κ to [1 60] W m^{-2} K^{-1}. Similarly, the oceanic heat flux F_w also needs to be estimated. According to Lei and others (2010), we set F_w approximately as the product of an annual sinusoidal function (F_w reaches a maximum of 16 W m^{-2} in mid-February and a minimum of 1 W m^{-2} in mid-August, Figure 9f) and a factor γ. The optimal value of oceanic heat flux can be obtained by optimally estimating the factor γ. In summary, refer to the manual surface drilling measurements, we estimate the optimal values by varying snow coefficient β, air-snow effective heat transfer coefficient κ and oceanic heat flux factor γ, while keeping the other parameters fixed.

Figure 9 shows the sea-ice thickness and growth rate based on Stefan's law (only the periods with the existence of surface drilling measurements) as well as the corresponding drilling measurements of freeboard, daily growth rate, surface air temperature, snow depth and default oceanic heat flux. The black solid line in Figure 9a is the sea-ice growth curve calculated using the optimal parameters. The values of snow coefficient β, oceanic heat flux factor γ and air-snow effective heat transfer coefficient κ are 1.07, 0.55 and 5.80, respectively (Fig. S3). The grey solid lines are the sea-ice growth curves of the best 1% parameter combination, in which the ranges of snow coefficient β, oceanic heat flux factor γ and air-snow effective heat transfer coefficient κ are [0.85 1.34], [0.11 1.0] and [4.6 7.5], respectively (Fig. S3). The growth rate of sea-ice thickness (Fig. 9c) is inversely correlated with the surface air temperature (Fig. 9d). The lower (higher) the surface air temperature is, the faster (slower) is the growth rate of sea ice. The snow depth on the surface of sea ice (Fig. 9e) also has a significant effect on the growth rate of sea ice. The growth rate of sea ice is relatively slow during the snow cover period (after DOY 180), and the deeper the snow depth is, the slower is the growth rate of sea ice. This is because the presence of snow insulates the heat exchange between air and sea ice. The optimum snow coefficient $\beta = \alpha/\lambda_s$ is 1.07 (the range of the best 1% is [0.85 1.34]). Considering that the value range of snow thermal conductivity λ_s is [0.07 0.45], the value of snow depth factor α is ~[0.07 0.48], which is <1. This simulation result also proves that there is snow overaccumulation at the drilling points, which is consistent with the field observations. The RMSE of the optimal sea-ice thickness curve simulated based on Stefan's law and manual drilling measurements is 4.74 cm. We used this simulated sea-ice thickness for the follow-up study.

5.3 Hydrostatic equilibrium at a single point

We use the 24-h median of freeboard time series calculated from solution 1 (TRACK + BPG tide + dynamic topography) as the daily freeboard, combined with the daily snow depth from the GPS-IR inversion and the simulated sea-ice thickness, to calculate the buoyancy of sea water to sea ice and the total weight of sea ice and snow to study whether the hydrostatic equilibrium is satisfied:

$$\rho_w h_d = \rho_i (h_f + h_d) + \rho_s h_s \quad (10)$$

where $\rho_w = 1.028$ g cm^{-3}, $\rho_i = 0.92$ g cm^{-3}, and $\rho_s = 0.32$ g cm^{-3} are the density of sea water, sea ice and snow, respectively. h_d, h_f, and h_s are the sea-ice draft, sea-ice freeboard and snow depth, respectively. Based on the hydrostatic equilibrium, the buoyancy of sea water to the sea ice equals to the total weight of sea ice and snow. Figure 10 shows the buoyance and total weight of the measured and calculated results and their relationship with hydrostatic equilibrium (dashed line). The closer the data points are to the dashed line, the more satisfied the hydrostatic equilibrium is. The manual drilling measurements with longer observation periods satisfy the hydrostatic equilibrium relationship on the whole scale, but there are anomalous points where the total weight is larger than the buoyancy. The reason why the total weight is greater than the buoyancy may be the abnormal snow depth at the drilling points. For the freeboard and snow depth derived from floating GPS and the simulated sea-ice thickness based on Stefan's law, there are some obvious

https://doi.org/10.1017/aog.2020.41 Published online by Cambridge University Press

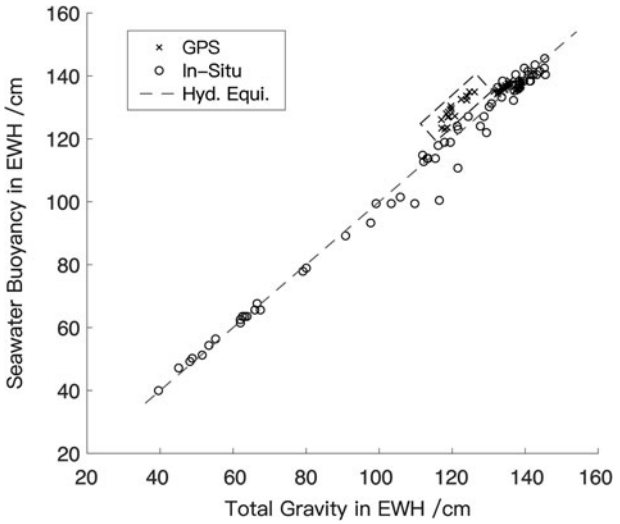

Fig 10. Buoyancy of sea water to sea ice and the total weight of sea ice and snow, and their relationship with hydrostatic equilibrium.

anomalies with their buoyancy greater than total weight even considering the freeboard deviation with respect to the drilling measurements (dotted box in Fig. 10). These abnormal points are all negative sea-ice freeboard points. Based on the hydrostatic equilibrium, the sea-ice thickness calculated using negative sea-ice freeboard is only ~60 cm, but the differences between the sea-ice thickness calculated from the hydrostatic equilibrium and the ones simulated using Stefan's law are ~60 cm, which means that the negative freeboards greatly underestimate the sea-ice thickness. The results show that it is unreliable to retrieve sea-ice thickness using single-point freeboard and snow depth based on the assumption of hydrostatic equilibrium, especially in the Southern Ocean where negative freeboard is common. We list three possible reasons why our experimental results do not meet the hydrostatic equilibrium. First, the land-fast sea ice along the coast may be squeezed by the peripheral sea ice. The deformation caused by squeezing may cause the ice surface in the study area to be bent below the sea surface. Second, the snow depth inverted by GPS-IR is only a small area near the GPS antenna, which cannot correctly reflect the snow depth over the entire sea-ice surface and thus underestimate the entire weight of snow. Third, the existence of flooded and refrozen snow, as well as other snow types, may complicate the snow weight calculation; thus, the nominal snow density could underestimate the entire snow weight over the sea ice. Due to the lack of upper and lower surface geometry of sea ice, as well as the entire snow depth and density, it is impossible to determine or distinguish which reason cause the phenomenon of negative freeboard. The spatial distribution of snow in the experimental area, as well as the geometry of the upper surface can be effectively monitored by deploying a GPS network on sea ice. Combined with the sea-ice draft obtained by the ULS or sea-ice thickness obtained by ice radar and the in-depth investigation of the snow types and densities, it is possible to determine the reason why the negative freeboard commonly exists on the Southern Ocean.

6. Conclusions

As a promising technology, altimeters can monitor the large-scale variation of sea-ice thickness in the Southern Ocean. However, altimeters face the difficulties of distinguishing the sea-ice freeboard from snow and the lack of in situ data to verify its accuracy and reliability. In this paper, we use a floating GPS deployed on the sea ice in the Nella Fjord, Antarctica, to derive and monitor the freeboard and snow depth. Through comparison with surface drilling measurements, the stand-alone floating GPS can continuously observe the freeboard variations in real time with a precision of ~4.2 cm. If there is time-varying dynamic topography information provided by other methods, such as a bottom pressure gauge, the precision of the freeboard retrieval (using the relative positioning results from TRACK plus the ocean tides and time-varying dynamic topography from BPG) can reach 1.3 cm, which is equivalent to the accuracy of surface drillings. The snow depth obtained by GPS-IR can effectively monitor the snow depth changes caused by precipitation and drifting near floating GPS receiver. Our experiment shows that a floating GPS (or a network) deployed on the ground track of altimeters can achieve synchronous observation with an altimeter; with the help of, for example, a tide gauge, the accuracy of altimeter-derived sea-ice freeboard can be assessed. Even if the study area has no dynamic topography information or where freeboard is thinner than the precision of GPS-derived freeboard (<4 cm), the stand-alone floating GPS can still help to separate snow from freeboard, which is the premise of using altimeters to invert sea-ice thickness. By studying the relationship between freeboard, snow depth, and sea-ice thickness, we find that a single-point measurement cannot satisfy the hydrostatic equilibrium. Under the assumption of hydrostatic equilibrium, the sea-ice thickness will be greatly underestimated by the negative freeboard. As an effective supplement to the existing observations, the variations of freeboard and snow depth observed by floating GPS can be used to directly verify the observations of altimeters and to improve our understanding of the real-time variations of freeboard and snow depth in the experimental area.

Supplementary material. The supplementary material for this article can be found at https://doi.org/10.1017/aog.2020.41.

Acknowledgements. We thank the Chinese 33rd Antarctic Scientific Research Zhongshan overwintering team for the field support. Q. Z., F. L., S. Z., and W. L. are financially supported by the Grants from the National Key Research and Development Program of China (2017YFA0603104), the State Key Program of National Natural Science Foundation of China (41531069) and the Independent Scientific Research Program for Cross-disciplinary of Wuhan University (2042017kf0209). J. L. and W. C. are supported by the Grants from the National Key Research and Development Program of China (2016YFB0501803) and the Hong Kong RGC Joint Research Scheme (E-PolyU501/16).

References

Abdalati W and 16 others (2010) The ICESat-2 laser altimetry mission. *Proceedings of the IEEE* **98**(5), 735–751.

Allison I (1981) Antarctic sea-ice growth and oceanic heat flux. *Sea Level, Ice and Climatic Change* **131**, 161–170.

Aoki S, Shibuya K, Masuyama A, Ozawa T and Doi K (2002) Evaluation of seasonal sea level variation at Syowa Station, Antarctica, using GPS observations. *Journal of Oceanography* **58**(3), 519–523.

Armitage TW and Ridout AL (2015) Arctic sea-ice freeboard from AltiKa and comparison with CryoSat-2 and operation IceBridge. *Geophysical Research Letters* **42**(16), 6724–6731.

Axelrad P, Larson K and Jones B (2005) Use of the correct satellite repeat period to characterize and reduce site-specific multipath errors. *Proceedings of the ION GNSS*, September, pp. 2638–2648.

Behrendt A, Dierking W, Fahrbach E and Witte H (2013) Sea-ice draft in the Weddell Sea, measured by upward looking sonars. *Earth System Science Data* **5**(1), 209–226.

Behrendt A, Dierking W and Witte H (2015) Thermodynamic sea-ice growth in the central Weddell Sea, observed in upward-looking sonar data. *Journal of Geophysical Research: Oceans* **120**(3), 2270–2286.

Cavalieri DJ and Parkinson CL (2008) Antarctic sea-ice variability and trends, 1979–2006. *Journal of Geophysical Research: Oceans* **113**(C7). doi: 10.1029/2007JC004558.

Comiso JC and Nishio F (2008) Trends in the sea-ice cover using enhanced and compatible AMSR-E, SSM/I, and SMMR data. *Journal of Geophysical Research: Oceans* **113**(C2). doi: 10.1029/2007JC004257.

Dushaw BD and 5 others (1997) A TOPEX/POSEIDON global tidal model (TPXO.2) and barotropic tidal currents determined from long-range acoustic transmissions. *Progress in Oceanography* **40**(1–4), 337–367.

Farrell SL and 9 others (2011) A first assessment of IceBridge snow and ice thickness data over Arctic sea-ice. *IEEE Transactions on Geoscience and Remote Sensing* **50**(6), 2098–2111.

Ferrari R and 5 others (2014) Antarctic sea-ice control on ocean circulation in present and glacial climates. *Proceedings of the National Academy of Sciences* **111**(24), 8753–8758.

Fu Y, Argus DF and Landerer FW (2015) GPS As an independent measurement to estimate terrestrial water storage variation in Washington and Oregon. *Journal of Geophysical Research: Solid Earth* **120**(1), 552–566.

Geng J and 6 others (2019) PRIDE PPP-AR: an open-source software for GPS PPP ambiguity resolution. *GPS Solutions* **23**(4), 91

Giles KA and 8 others (2007) Combined airborne laser and radar altimeter measurements over the Fram Strait in May 2002. *Remote Sensing of Environment* **111**(2–3), 182–194.

Giles KA, Laxon SW and Ridout AL (2008) Circumpolar thinning of Arctic sea-ice following the 2007 record ice extent minimum. *Geophysical Research Letters* **35**, 22.

Griesel A, Mazloff R and Gille ST (2012) Mean dynamic topography in the Southern Ocean: evaluating Antarctic circumpolar current transport. *Journal of Geophysical Research: Oceans* **117**, C1.

Herring TA, King RW and McClusky SC (2010) *Introduction to Gamit/Globk*. Cambridge, Massachusetts: Massachusetts Institute of Technology.

Huang J and Zhang S (2012) Zero calibration of bottom pressure gauge in Antarctic: a case study at Chinese Zhongshan station using GPS techniques. *20th International Conference on Geoinformatics*, June, pp. 1–4. IEEE.

Kaleschke L, Tian-Kunze X, Maaß N, Mäkynen M and Drusch M (2012) Sea-ice thickness retrieval from SMOS brightness temperatures during the Arctic freeze-up period. *Geophysical Research Letters* **39**(5). doi: 10.1029/2012GL050916.

King MA and 7 others (2009) A 4-decade record of elevation change of the Amery Ice Shelf, East Antarctica. *Journal of Geophysical Research: Earth Surface* **114**(F1). doi: 10.1029/2008JF001094.

King M and Aoki S (2003) Tidal observations on floating ice using a single GPS receiver. *Geophysical research letters* **30**(3). doi: 10.1029/2002GL016182.

Kurtz NT (2013) Sea-ice thickness, freeboard, and snow depth products from Operation IceBridge airborne data. *The Cryosphere* **7**(4), 1035–1056.

Kurtz NT, Galin N and Studinger M (2014) An improved CryoSat-2 sea-ice freeboard retrieval algorithm through the use of waveform fitting. *The Cryosphere* **8**(4), 1217–1237.

Kurtz NT and Markus T (2012) Satellite observations of Antarctic sea-ice thickness and volume. *Journal of Geophysical Research: Oceans* **117**(C8). doi: 10.1029/2012JC008141.

Kwok R (2018) Arctic sea-ice thickness, volume, and multiyear ice coverage: losses and coupled variability (1958–2018). *Environmental Research Letters* **13**(10), 105005.

Kwok R and 8 others (2019) ICESat-2 surface height and Sea Ice freeboard assessed With ATM Lidar acquisitions from operation IceBridge. *Geophysical Research Letters* **46**(20), 11228–11236.

Kwok R, Cunningham GF, Manizade SS and Krabill WB (2012) Arctic sea-ice freeboard from IceBridge acquisitions in 2009: estimates and comparisons with ICESat. *Journal of Geophysical Research: Oceans* **117**(C2). doi: 10.1029/2011JC007654.

Kwok R, Cunningham GF, Zwally HJ and Yi D (2007) Ice, Cloud, and land Elevation Satellite (ICESat) over Arctic sea-ice: retrieval of freeboard. *Journal of Geophysical Research: Oceans* **112**(C12). doi: 10.1029/2006JC003978.

Kwok R and Kacimi S (2018) Three years of sea-ice freeboard, snow depth, and ice thickness of the Weddell Sea from operation IceBridge and CryoSat-2. *The Cryosphere* **12**(8), 2789–2801.

Kwok R and Rothrock DA (2009) Decline in Arctic sea-ice thickness from submarine and ICESat records: 1958–2008. *Geophysical Research Letters* **36**, 15.

Larson KM (2009) GPS Seismology. *Journal of Geodesy* **83**(3–4), 227–233.

Larson KM (2016) GPS Interferometric reflectometry: applications to surface soil moisture, snow depth, and vegetation water content in the western United States. *Wiley Interdisciplinary Reviews: Water* **3**(6), 775–787.

Laxon SW and 14 others (2013) Cryosat-2 estimates of Arctic sea-ice thickness and volume. *Geophysical Research Letters* **40**(4), 732–737.

Lei J and 7 others (2018) Ocean tides observed from A GPS receiver on floating sea ice near Chinese Zhongshan station, Antarctica. *Marine Geodesy* **41**(4), 353–367. doi: 10.1080/01490419.2018.1454370.

Lei R, Li Z, Cheng B, Zhang Z and Heil P (2010) Annual cycle of landfast sea-ice in Prydz Bay, east Antarctica. *Journal of Geophysical Research: Oceans* **115**(C2). doi: 10.1029/2008JC005223.

Leppäranta M (1993) A review of analytical models of sea-ice growth. *Atmosphere-Ocean* **31**(1), 123–138.

Maksym T (2019) Arctic and Antarctic sea ice change: contrasts, commonalities, and causes. *Annual Review of Marine Science* **11**, 187–213.

Massom RA and 13 others (2001) Snow on Antarctic sea-ice. *Reviews of Geophysics* **39**(3), 413–445.

Meehl GA and 7 others (2019) Sustained ocean changes contributed to sudden Antarctic sea ice retreat in late 2016. *Nature Communications* **10**(1), 1–9.

Naoki K and 5 others (2008) Thin sea-ice thickness as inferred from passive microwave and in situ observations. *Journal of Geophysical Research: Oceans* **113**(C2). doi: 10.1029/2007JC004270.

Parkinson CL and DiGirolamo NE (2016) New visualizations highlight new information on the contrasting Arctic and Antarctic sea-ice trends since the late 1970s. *Remote Sensing of Environment* **183**, 198–204.

Peng G, Meier WN, Scott DJ and Savoie MH (2013) A long-term and reproducible passive microwave sea-ice concentration data record for climate studies and monitoring. *Earth System Science Data* **5**(2), 311–318.

Petrich C and Eicken H (2010) Growth, structure and properties of sea-ice. *Sea-ice* **2**, 23–77.

Ricker R, Hendricks S, Helm V, Skourup H and Davidson M (2014) Sensitivity of CryoSat-2 Arctic sea-ice freeboard and thickness on radar-waveform interpretation. *The Cryosphere* **8**(4), 1607–1622.

Roesler C and Larson KM (2018) Software tools for GNSS interferometric reflectometry (GNSS-IR). *GPS Solutions* **22**(3), 80.

Schaffrin B and Bock Y (1988) A unified scheme for processing GPS dual-band phase observations. *Bulletin géodésique* **62**(2), 142–160.

Screen JA and Simmonds I (2010) The central role of diminishing sea-ice in recent Arctic temperature amplification. *Nature* **464**(7293), 1334.

Semmling AM and 9 others (2019) Sea-ice concentration derived from GNSS reflection measurements in fram strait. *IEEE Transactions on Geoscience and Remote Sensing* **57**(12), 10350–10361.

Siegfried MR, Medley B, Larson KM, Fricker HA and Tulaczyk S (2017) Snow accumulation variability on a West Antarctic ice stream observed with GPS reflectometry, 2007–2017. *Geophysical Research Letters* **44**(15), 7808–7816.

Simpkins GR, Ciasto LM, Thompson DW and England MH (2012) Seasonal relationships between large-scale climate variability and Antarctic sea-ice concentration. *Journal of Climate* **25**(16), 5451–5469.

Stroeve JC and 6 others (2012) Trends in Arctic sea-ice extent from CMIP5, CMIP3 and observations. *Geophysical Research Letters* **39**(16). doi: 10.1029/2012GL052676.

Sturm M, Morris K and Massom R (1998) The winter snow cover of the West Antarctic pack ice: its spatial and temporal variability. *Antarctic Sea Ice: Physical Processes, Interactions and Variability* **74**, 1–18.

Wadhams P (2014) *Ice in the Ocean*. USA: CRC Press.

Warren SG and 6 others (1999) Snow depth on Arctic sea-ice. *Journal of Climate* **12**(6), 1814–1829.

Webster MA and 6 others (2014) Interdecadal changes in snow depth on Arctic sea-ice. *Journal of Geophysical Research: Oceans* **119**(8), 5395–5406.

Worby AP and Comiso JC (2004) Studies of the Antarctic sea-ice edge and ice extent from satellite and ship observations. *Remote Sensing of Environment* **92**(1), 98–111.

Xia W and Xie H (2018) Assessing three waveform retrackers on sea-ice freeboard retrieval from Cryosat-2 using operation IceBridge Airborne altimetry datasets. *Remote Sensing of Environment* **204**, 456–471.

Zhang J, Lindsay R, Schweiger A and Rigor I (2012) Recent changes in the dynamic properties of declining Arctic sea-ice: a model study. *Geophysical Research Letters* **39**(20). doi: 10.1029/2012GL053545.

Zhao J, Cheng B, Yang Q, Vihma T and Zhang L (2017) Observations and modelling of first-year ice growth and simultaneous second-year ice ablation in the Prydz Bay, East Antarctica. *Annals of Glaciology* **58**(75 pt1), 59–67.

Zwally HJ, Yi D, Kwok R and Zhao Y (2008) ICESat measurements of sea-ice freeboard and estimates of sea-ice thickness in the Weddell Sea. *Journal of Geophysical Research: Oceans* **113**(C2). doi: 10.1029/2007JC004284.

https://doi.org/10.1017/aog.2020.41 Published online by Cambridge University Press